ADVANCES IN MATERIALS SCIENCE, Vol. 19, No. 2 (60), June 2019

DOI: 10.2478/adms-2019-0011

B. Trybuś[1], J. M. Olive[2], N. Lenoir[3], A. Zieliński[1]*

[1] *Gdansk University of Technology, Faculty of Mechanical Engineering, Department of Materials Science and Welding Engineering, Narutowicza 11/12, 80-233 Gdańsk, Poland*
[2] *C.N.R.S., I2M, UMR 5295, 351 cours de la Liberation, Talence 33405, France*
[3] *PLACAMAT : Plateforme Aquitaine de Caractérisation des Matériaux: UMS C.N.R.S. 3626, 87 Av. Du Dr. A. Schweitzer, 33600 Pessac, France*
* *azielins@pg.edu.pl*

X-RAY COMPUTER TOMOGRAPHY STUDY OF DEGRADATION OF THE ZIRCALOY-2 TUBES OXIDIZED AT HIGH TEMPERATURES

ABSTRACT

The investigations of high-temperature oxidation of zirconium alloys, applied for fuel pellets in nuclear power plants, are usually limited to oxidation kinetics, phase transformations and microstructural characterization. The purpose of this research was to characterize the degradation phenomena occurring within oxide layer and at the interface oxide/metal, on internal and external Zircaloy-2 tube surfaces, below and over crystalline transformation temperature of zirconium oxides. The commercial tubes were oxidized at 1273 K and 1373 K in calm air for 30 min and then examined with a technique novel for such purpose, namely a high-resolution X-ray computer tomography. The light microscopy was used to examine the cross-surfaces. The obtained results show that the form and intensity of oxide damage is significant and it is in a complicated way related to oxidation temperature and on whether external or internal tube surface is studied. The found oxide layer damage forms include surface cracks, the detachment of oxide layers, the appearance of voids, and nodular corrosion. The oxidation effects and damage appearance are discussed taking into account the processes such as formation of oxides, their phase transformation, stress-enhanced formation and propagation of cracks, diffusion of vacancies, formation of nitrides, diffusion of hydrogen into interface oxide-metal, incubation of cracks on second phase precipitates are taken into account to explain the observed phenomena.

Keywords: *zirconium, oxide layers, high temperature, X-ray tomography, cracking, nodular corrosion*

INTRODUCTION

The zirconium and its alloys are heat-resistant materials used among others in the nuclear industry for fuel claddings. Its degradation in high temperatures depends on a variety of determinants such as an oxidation temperature, oxidation time, environment composition, heating and cooling rates, material composition, surface state, presence and level of residual stresses. Effect of temperature is prevalent and associated with three factors: (i) an oxide growth dependent on temperature and oxygen partial pressure, (ii) phase transformation of oxides into different crystalline structures, and (iii) damage of the oxide layer [1,2].

The oxidation of Zr alloys is mainly represented by parabolic rate correlation [3], which is unsuitable for long-term isothermal oxidation or when oxidation occurs under steam starvation conditions. The oxidation made up to 1273 K temperature results in a change from sub-parabolic to linear or even faster kinetics, where at 1373 K and higher temperatures, no such further transition occurs [4,5].

Both the monoclinic and tetragonal phases can be formed even at 623 K temperature, their volume fractions increasing until 1273 K where the α phase disappears completely [6]. For Zircaloy-2, the crystal structures appear as Zr > Zr_3O > tetragonal ZrO_2 > monoclinic ZrO_2 from the matrix to the surface [7]. For a Zircaloy-4 alloy oxidized at 673 K in steam, the monoclinic columnar grains form inner oxide zone, and porous equiaxed grains are outer oxides [8]. At 923 K, the dominant phase is still monoclinic ZrO_2 in a columnar form [9,10]. Between 1073 and 1373 K, both tetragonal and monoclinic zirconia phases exist during oxide growth, above 1323 K only tetragonal phase is seen. The grain size of the tetragonal zirconia is about 100 nm at 1373 K and only 20 nm after cooling down to room temperature [11,12]. The oxidation at high temperature causes the breakaway effect dependent on oxidation temperature and time [13-16]. For example, for the Zircaloy-4 exposed to steam and oxidized at 1273 K, the breakaway oxidation was observed after more than 1500 s in the ruptured fuel cladding and after more than 3600 s in the non-ruptured alloy [14].

The chemical composition and alloy morphology, and, in particular, a presence of second phase precipitates (SPPs), is essential for the oxide growth, characteristics and behavior [1]. For Zircaloy-4 and Zirlo oxidized at 973-1473 K under steam supply condition for 3600 s, the weight gain rates of Zirlo were lower than those of Zircaloy-4 [17]. The formation of a relatively thick oxide layer on the new Zr-2Mn alloy was observed already after oxidation at 623 K thanks to a high affinity of oxygen to manganese [18]. The breakaway oxidation time was shortened with an increase in the Sn content in the Zr alloys [13]. In Zircaloy-4, the oxidation of the Zr_2Fe and the $Zr(Fe, Cr)_2$ SPPs proceeded differently [19]. For the tin-bearing alloy Zircaloy-4 and the niobium-bearing alloy E110 the temperature range, at which clear breakaway was observed, was different [4].

The degradation mechanisms related to the oxidation may occur, such as a uniform corrosion of thin ZrO2 layers, nodular corrosion due to formation of local small circular oxide blisters, shadow corrosion due to formation of local corrosion regions that mirror the shape of core components [2,20], and the cracking of oxide layers typical of high temperatures. The rapid transformation of tetragonal oxide to monoclinic oxide is likely the main reason for the appearance of poor-quality monoclinic oxide [3]. The circumferential cracks at the oxide/metal interface decrease the oxidation rate by limiting the oxygen diffusion before the breakaway oxidation start [21]. For the E110 alloy, the fracture started with the formation of brittle cracks 30–50 µm long in the α-layer, which then propagated simultaneously into the oxide and prior β-layers [22]. The appearance of cracks both before and after the transition in kinetics and not a sudden burst of crack nucleation at transition was observed [23,24].

This research was aimed at further characterization of the behavior of oxidation and degradation of oxide layers formed at relatively high temperature, in particular shortly before and after a kinetic transition. Such research, made by the X-ray tomography, has never been performed and it makes it able to precisely and in non-destructive way, characterize the oxide layer degradation, both on surface and at the oxide/metal interface.

MATERIALS AND METHODS

Oxidation was performed on commercial (Sandvik) as-received Zircaloy-2 tubes without any further surface polishing. The chemical composition of the alloy was (in mass pct.): 1.37 Sn, 0.18 Fe, 0.11 Cr, 0.07 Ni, 0.37 Fe+Cr+Ni, 0.013 C, 0.0092 Si, 1184 ppm O, Zr the remainder. The tubes had an external diameter of 12 mm and a wall thickness of 0.77 mm. Samples of 5 mm long were cut for oxidation tests. Specimens were cleaned in distilled water and ethanol and dried in air.

Oxidation was performed at 1273 K and 1373 K in calm air of atmospheric pressure and humidity at the Carbolite ELF 11/6b electric furnace. The specimens were oxidized for 30 min in an already heated furnace to introduce some thermal stresses. The oxygen starvation was assessed at below 5% so that it could not significantly affect the oxidation kinetics. The tubes were then taken out of the furnace and cooled at a different rate in either ambient air, water, and commercial synthetic oil to separate the damage due to oxidation from that caused by thermal stresses. The cooling time to room temperature was around 2 min.

The X-ray tomography method was applied to examine the damage because of its high resolution and non-destructive form. The resolution was either 14 μm or 1.4 μm in some tests made on more damaged surfaces. The tests were performed using the X-ray Versa XRM-500 (Zeiss-Xradia) tomography. The measurement parameters for the 14 μm voxel size were the X-ray source voltage 150 kV, power 10 W, exposure time 6 s, magnification 0.39x, source filter HE3, and for the 1.4 μm voxel size 150 kV, 10 W, 50 s, 4x, HE5, alternatively. For both magnifications, the 1600 projections were recorded.

The images were analyzed using the ImageJ program. Fig. 1 illustrates a scheme examination procedure. Some voxels were quantified, based on the scan resolution, to compare the oxide layers and base metal (Fig. 1a). Every scan was separated into three sections. The quantifications of oxidized specimens were based on 100 slices (1400 μm height) separated from the middle section of the scanned tube, and on 80 slices (1120 μm height) for the top and bottom sections. Fig. 1b, c shows three different sections of a specimen and separate oxide layers, alternatively. The view of transverse cross-sections and their binary images are illustrated in Fig. 1 d, e, f.

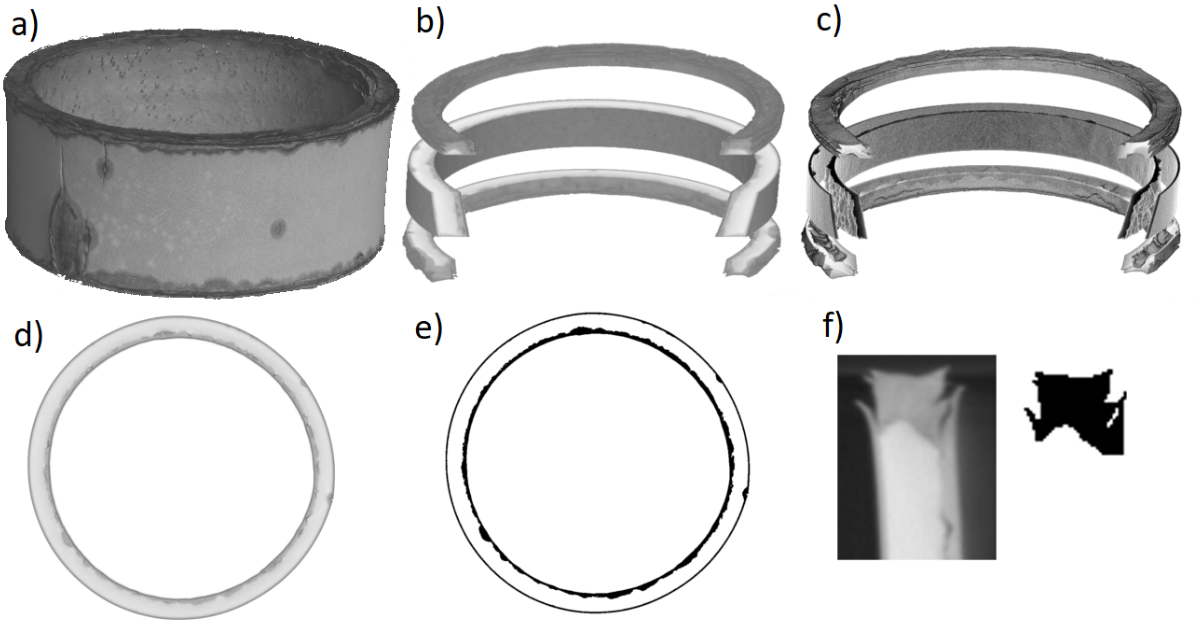

Fig. 1. a) X-ray tomography made the 3D view of sample oxidized at 1373 K and cooled in air, b) separated zones of an oxidized metal, c) separated zones of an oxide layer, d) view of the single slice of the transverse cross-section of the tube; **e)** binary image of the transverse cross-section of the tube, outer and inner oxide layers can be recognized, f) longitudinal cross-section of the tube and its binary image, the oxide layer at the top edge can be seen.

The calculations of volume and thickness of the oxide layer were based on the middle section. The threshold color value was set up to obtain the binary images of the oxide - substrate material systems. The volumes of the oxide and substrate were calculated based on a volume of a single voxel, 2744 μm^3 at a scan resolution of 14 µm per voxel. The middle section had the volume of 40.1 mm^3, the outer surface area was 53.6 mm^2 and inner surface area was 46.6 mm^2. The density of oxide was assumed for further calculations as of 5.56 g/cm^2.

The cross-sections were examined with the light microscopy on specimens mechanically polished with the abrasive paper, No. 4000 as the last, and then electrochemically polished.

RESULTS AND DISCUSSION

Oxidation kinetics

Relationships between the volumes and thickness of the oxide layers, and oxidation temperature and a place of oxidation (oxides grown on the internal or external surface of the tube, called later inner and outer oxides) are presented in Fig. 2. The increasing temperature resulted in an increasing oxide volume and thickness. Both surfaces revealed similar thickness of oxide layer after oxidation at lower temperature, and higher on internal surface after oxidation at 1373 K.

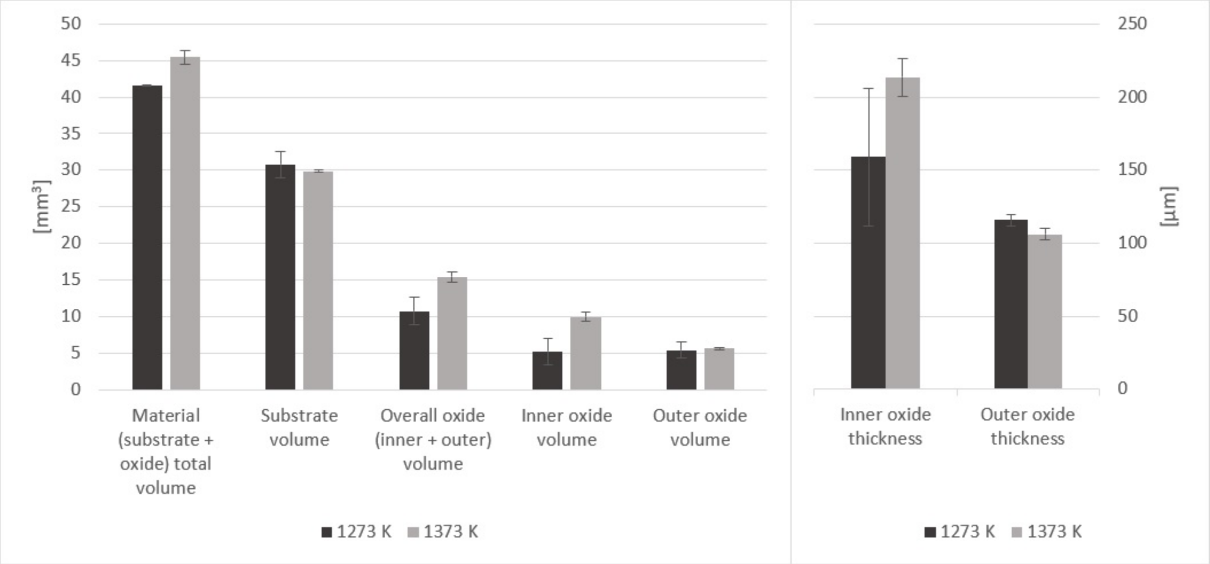

Fig. 2. Relation of the oxide layer volume and thickness on oxidation temperature and oxide layer placement (outside or inside the tube)

Specimens oxidized at 1273 K revealed multiple cracks in the oxide layers. The image analysis of micrographs shown in Fig. 3 discloses that the cracks occupy about 20% of oxide volume. From each image, two fragments, 0.01 mm^2 each, were taken and converted into binary images for calculation of the number of voxels and volume of cracks. Most cracks were not big enough to be directly visible on the X-ray tomography scans.

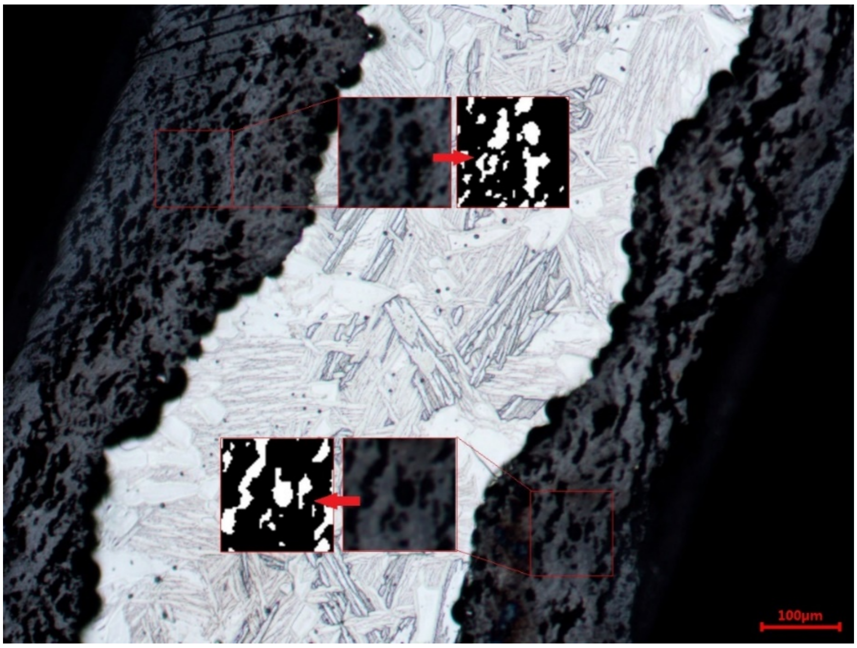

Fig. 3. Microscope images of a cross-section of Zircaloy-2 alloy oxidized at 1273 K in air and cooled in oil; the areas used for an assessment of cracks` number (small images, on the left) and their binary images (small images, on the right) and calculation of voxels` number are demonstrated

Based on the estimated number and volume of cracks in the oxide layer, the volume of oxide layer was arbitrarily reduced for each temperature and the place of layer, internal or external, e.g. about 20% for specimens oxidized at 1273 K. Figure 4 presents a change in mass per unit area in the middle section of the oxidized tube in comparison to the non-oxidized sample. The presented values were calculated based on the previously measured volumes of the middle section and volumes of oxide, and densities of the substrate alloy and the zirconium dioxide. The volume of reacted zirconium cladding determines previously oxidized part of the cladding.

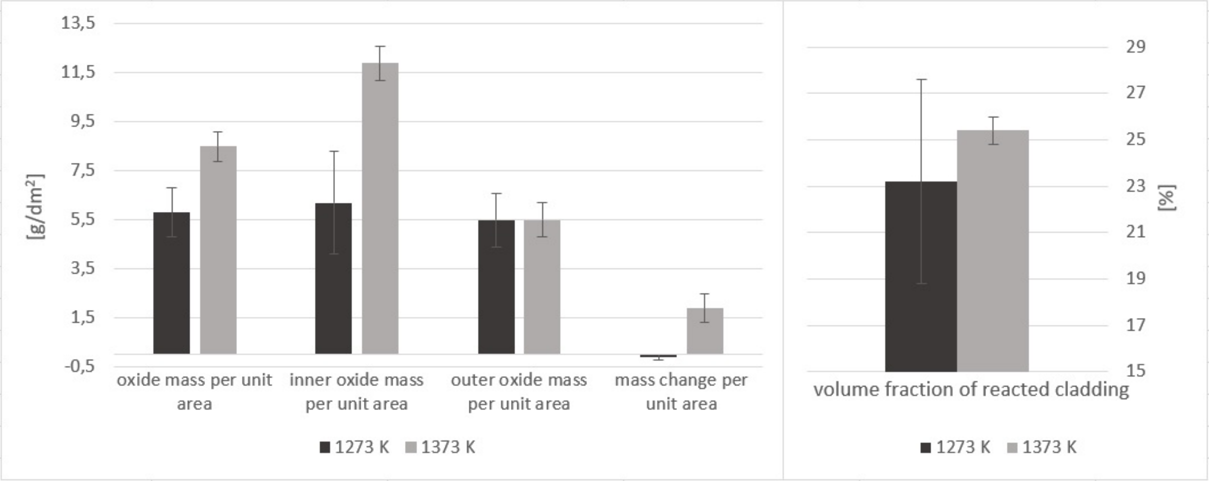

Fig. 4. *Oxide mass per unit area and volume fraction of reacted cladding obtained at different oxidation*

The weight gains are consistent with the reference values for oxidation temperature of 1273 K, but after oxidation at 1373 K, they are slightly lower than reported so far [4,5,25]. This discrepancy is negligible and may be attributed to the specimen`s geometry, different microstructure, difference between flat and curved surfaces, different environment (air instead of steam) and, in consequence, different oxide growth. The higher inner oxide thickness comparing to the outer oxide after oxidation at 1373 K is contradictory to some previous observations [26]. The origin of this difference is unclear. It may be an effect of substantial degradation of external surface due to nodular corrosion followed by defragmentation of the oxide. The compressive stresses, higher at internal surface, may decrease the oxygen diffusion into a bare metal; the lower oxygen solubility in metal, the faster oxide growth [27]. The most plausible explanation is that after oxidation at 1373 K, the severe degradation of oxide layers, more advanced in case of external layer, resulted in a partial loss of the layer during cooling.

Forms of oxide damage

Different forms of damage were observed after oxidation at different temperatures. The damage forms may be classified as the cracks, detachment of oxide layers, an appearance of (macro)voids at the interface, formation of nodules. The presentation of observed damage at different temperature is schematically shown in Table 1. The scans of the whole claddings after oxidation at different temperature and cooling in different media are illustrated in Fig. 5 and the particular forms damage are shown separately for specimens oxidized at 1273 K (Fig. 6) and 1373 K (Fig. 7), and cooled either in air or in water (after cooling in oil similar results were obtained).

Table 1. *Appearance of different degradation forms as related to oxidation temperature*

Oxidation temperature	Vertical cracks in the oxide layer	Detachment of the oxide layer	Voids in the substrate	Nodular corrosion
1273 K	Numerous cracks on both internal and external surfaces	Severe, only on external surface	No present	No present
1373 K	Single long cracks, visible only on external surfaces	Moderate	Present	Present, mainly on external surface

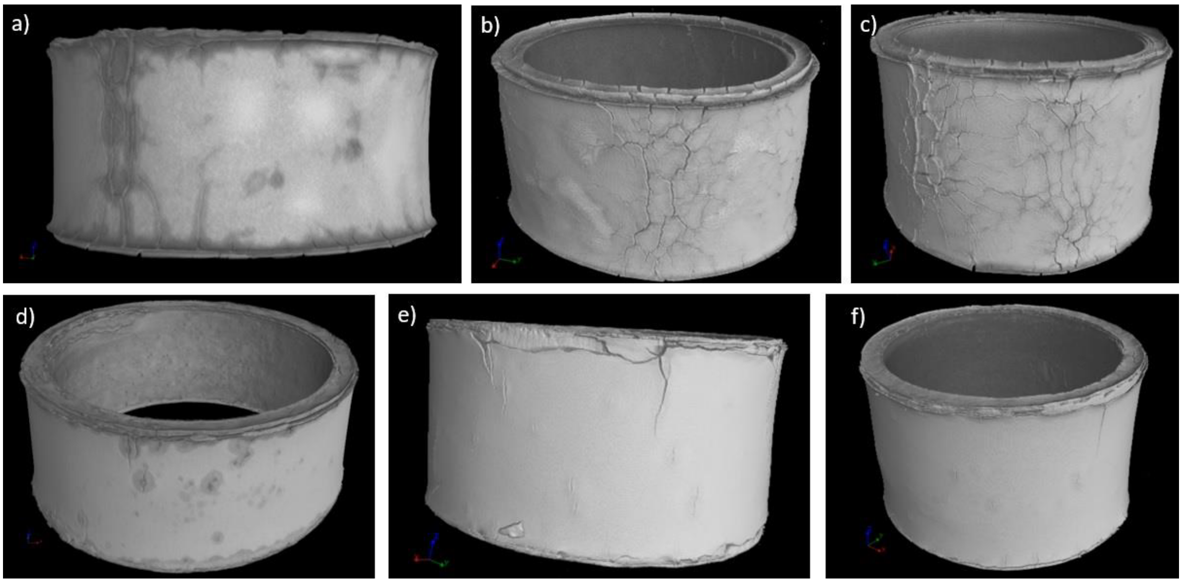

Fig. 5. Scans of the whole zirconium claddings after oxidation at 1273 K (top) and 1373 K (bottom) cooled in air (b, f), water (c, d) and oil (a, e)

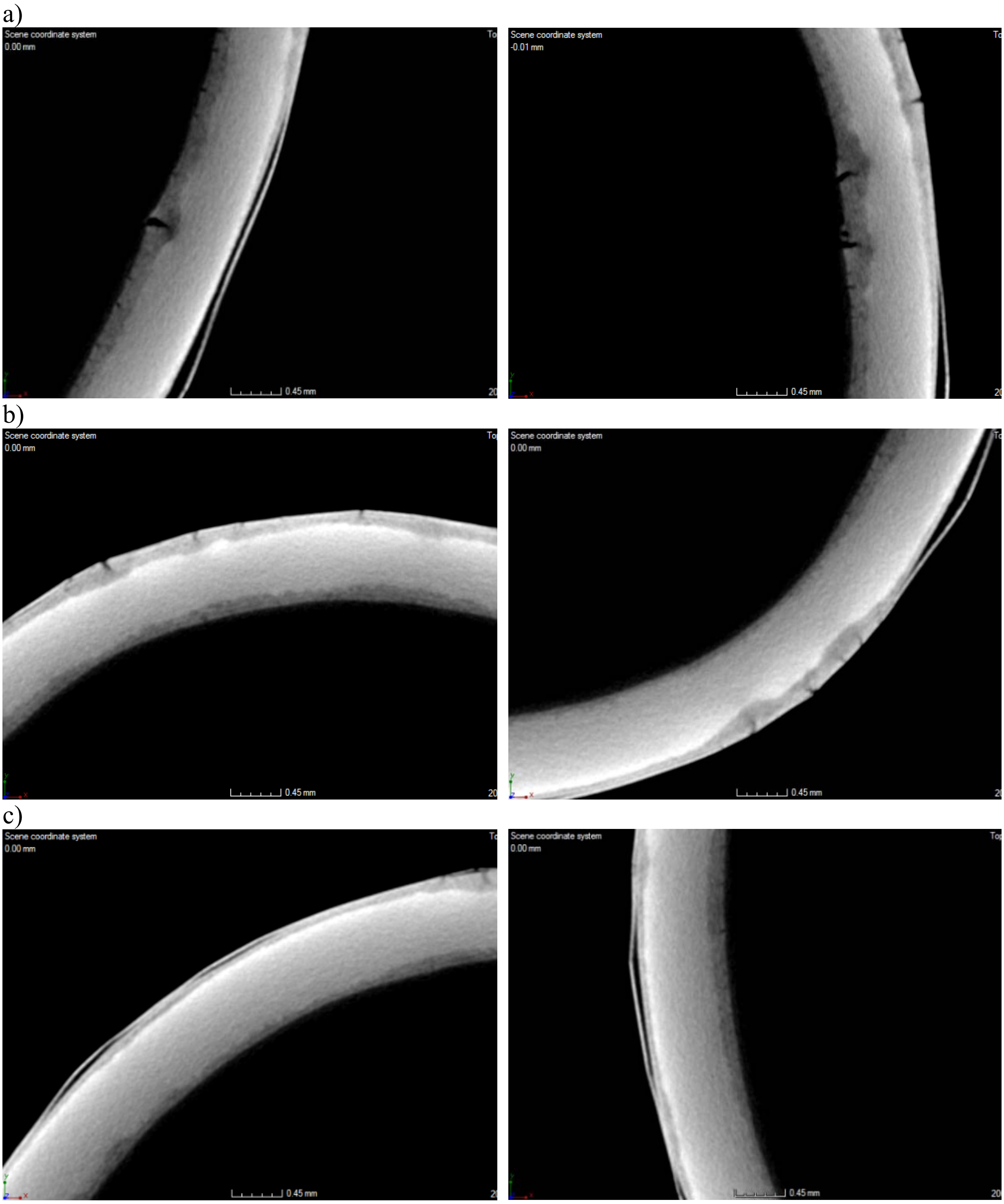

Fig. 6. Cross-sections of walls of tubes oxidized at 1273 K and cooled in air (left) or in water (right), different forms of degradation: a) vertical cracks in the inner oxide, b) vertical cracks in the outer oxide, c) detachment of the outer oxide (1273 K in air). Light microscope.

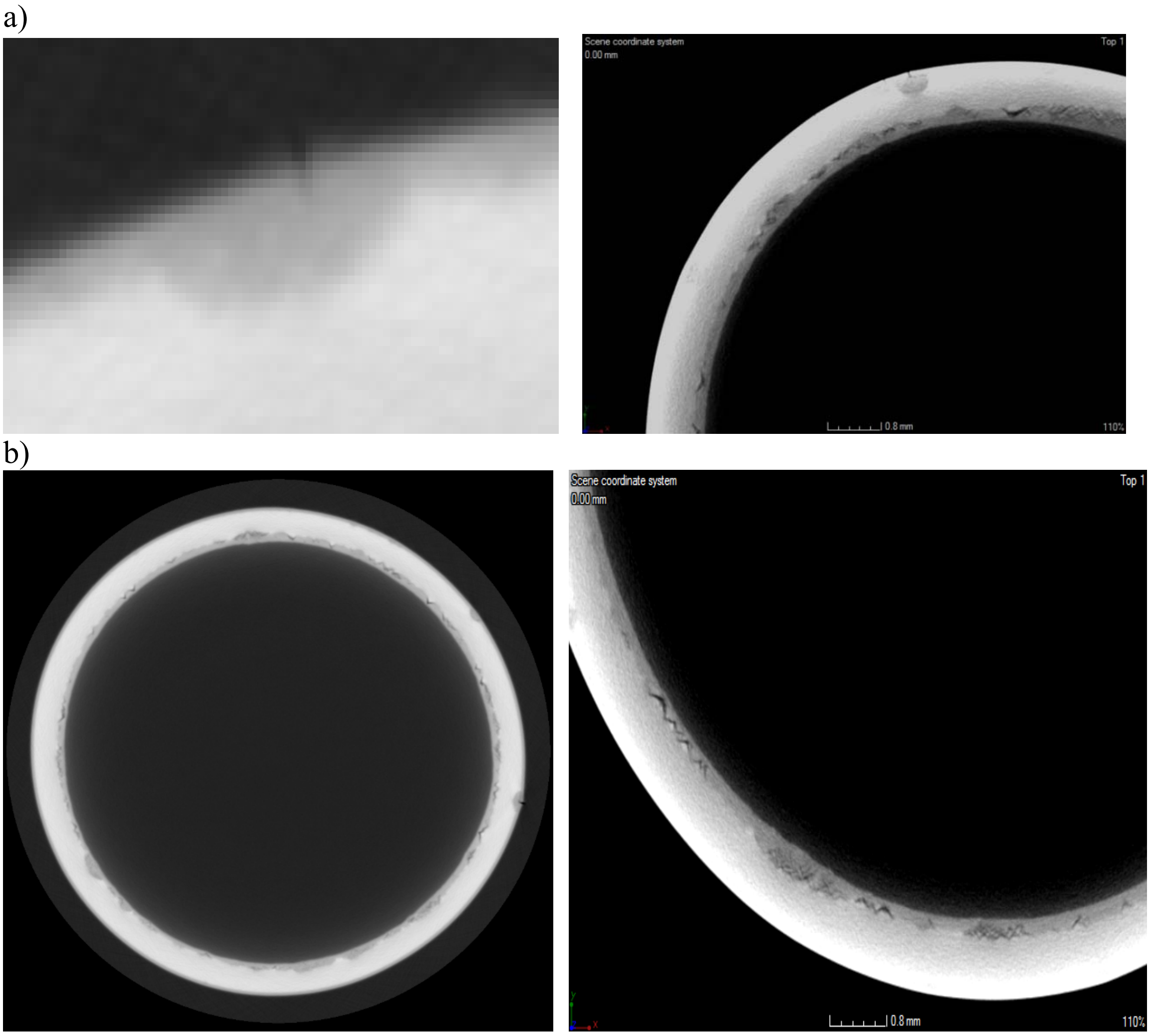

Fig. 7. Cross-sections of walls of tubes oxidized at 1373 K and cooled in air (left) or in water (right), different forms of degradation: a) vertical cracks in the oxide external layer, b) voids in the substrate. Light microscope

The observed damage was dependent on oxidation temperature and surface geometry of specimens (curved internal and external surfaces). The increase in temperature results in increased compressive stresses, the highest at the interface oxide/metal [26]. The stresses originated by different curvature of specimen have different effects: they are independent of temperature, compressive at internal surface of the oxide and longitudinal at external surface of the oxide. Besides, the phase transformation of oxides occurs between both chosen oxidation temperatures.

Oxidation at 1273 K

Degradation on external surface of the oxidized tubes appeared as long, spreading out and deep cracks or local, lens-like shaped small cracks. Figure 8 illustrates the long cracks observed on the alloy oxidized at 1273 K and cooled in water. The 3D views show that cracks join together and create island-like areas of size ranged from 400 μm to 1000 μm. The images on the left represent the cross-sections made along color lines marked in the middle image. The images on the right highlight the extensive oxide growth around cracks. Such behavior might be attributed to thermal stresses, but cooling medium did not affect the cracking intensity. The oxide near the vertical crack was locally very thick due to the direct exposure of inner oxide to the surrounding gases as already observed [3].

The appearance of long and deep cracks can be easily explained. The oxides have different crystalline form dependent on temperature and exist as monoclinic ZrO_2 at here applied lower oxidation temperatures [28], but evolution of small amounts of tetragonal phase was also reported between 623 K and 1223 K [6]. The oxide layers possess small columnar grains and equiaxed grains [4]. The cracking of oxide layers at relatively low oxidation temperature was often observed [29,30]. The cracking of the oxide layer was explained by the accumulation of compressive stresses in the oxide at the interface in pre-transition stage, resulting from imperfect accommodation of the volume expansion attendant upon oxide formation [2]. Two forms of cracks, circumferential and radial, were so far described [31]. The radial cracks forming the “snakeskin” surface, very similar to the present results, were attributed [27] to the sample growth by metal creep upon the tensile stress field applied by the growing oxide layer. It is also believed that, when the oxide growth continues, the external part of the oxide scale increases its distance from the interface, the compressive stress diminishes, which results in transition from tetragonal to monoclinic phase. When a total oxide thickness exceeds a given value, for zirconia is approx. 3 µm, the oxide layer begins to form lateral cracks only in the zone consisting from large, elongated grains in monoclinic phase [32]. The probable initiation site may be different second phase particle (SPP), in particular on their side opposite to the metal/oxide interface [1,19,33,34].

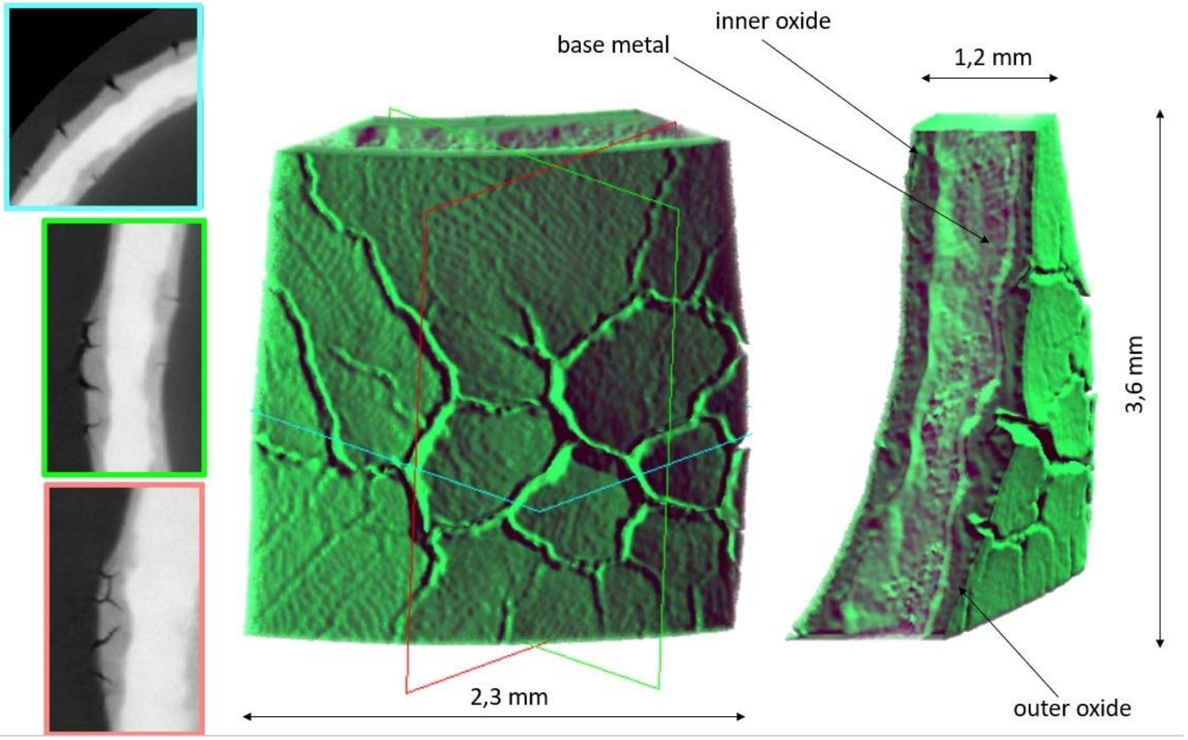

Fig. 8. 3D view of cracks spotted on outer oxide of Zircaloy-2 cladding oxidized at 1273 K for 30 min in air, cooled in water. On the left, grayscale images illustrate cross-sections made along color lines marked in the middle picture. The right image shows 3D view across the wall thickness which presents an increase in oxide thickness around cracks in comparison to an area without cracks

The cracks were scarce on inner tube surface. Such behavior may be understood when considering the stress state. On the outer surface, the highest compressive stresses appear at the interface metal – oxide and slowly decrease with a distance from the substrate [35]. On the contrary, on the inner surface the compressive stresses increase with a distance from the tube surface and these compressive stresses retard the crack initiation and propagation. However, the differences in air flow and temperature, not determined here, cannot be neglected.

Figure 9 presents an exemplary case of oxide detachment oxide observed for specimen oxidized at 1273 K and cooled in water. The spalled part of the layer was around 60 µm thick, and the oxide layer thickness ranged between 30 and 50 µm. The detached zone extended over an almost full area of the oxidized specimen. The green image in the middle illustrates an overall view of the oxide detachment. It visualizes bulge with a crack on the top. The image on the right shows the oxide under the detached layer. The image on the left presents orthogonal views of the area of interest. This form of detachment occurs in all the specimens oxidized at 1273 K. In all cases, the damage is sizable and exceeds 3 mm parallel to the tube and 2 mm perpendicular to the tube radius. Every specimen in this study possessed the crack or multiple cracks on the top of a bulge. The descaling, again much more intensive on the outer surface, is an obvious consequence of developing cracking as already observed [29].

The presence of compressive stresses, lower at internal and higher at external tube surface, may be another mechanism resulting in detachment of oxide layers and their cracking. The oxidation of possible hydrides, because oxidation in wet air, may also be considered as another possible mechanism of crack formation in the oxide [36].

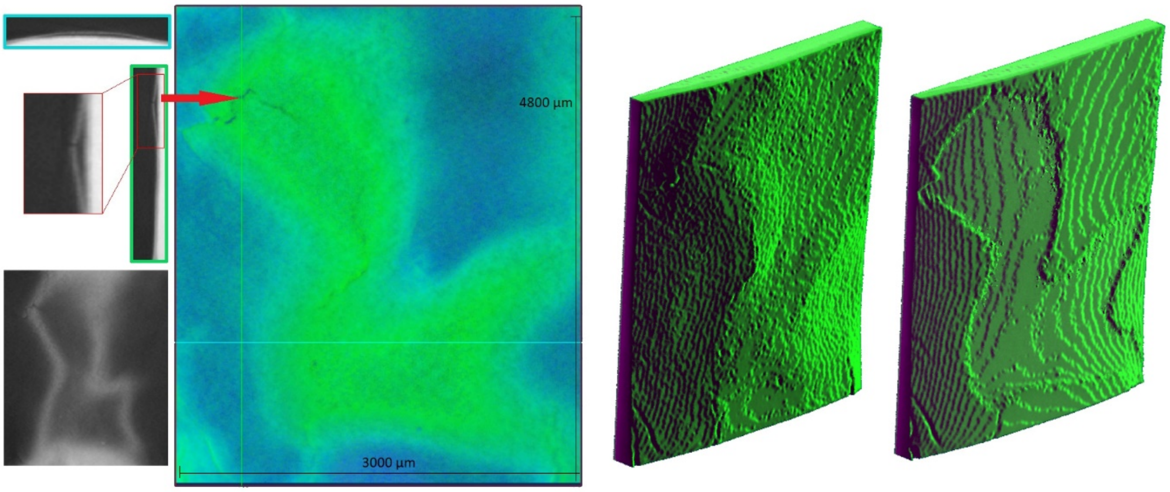

Fig. 9. Detachment of the outer oxide layer on specimen oxidized at 1273 K in air for 30 min and cooled in water. On the left: views of the scanned tube, blue and green lines on the bigger picture correspond to grayscale projections and show the area in which cross-sections were taken. On the right: two green images present 3D views of the detached oxide layer; the left of both shows the outer layer, the right of both illustrates the oxide layer under the detached part

Oxidation at 1373 K

In each sample oxidized at 1373 K, the triangle-like deformations were spotted on the whole inner surface under the oxide layer. As shown in Figs. 10-12, in the area of these deformations, the oxide layer was much thinner, and the cracks and large size voids were created at the interface metal - oxide. As the void, the space between oxide layer and substrate is assumed.

Fig. 10 shows a grey-level difference between the tops of the bright triangle-like deformations at the interface. Such bright areas are visible at the tops of most of the appearing voids.

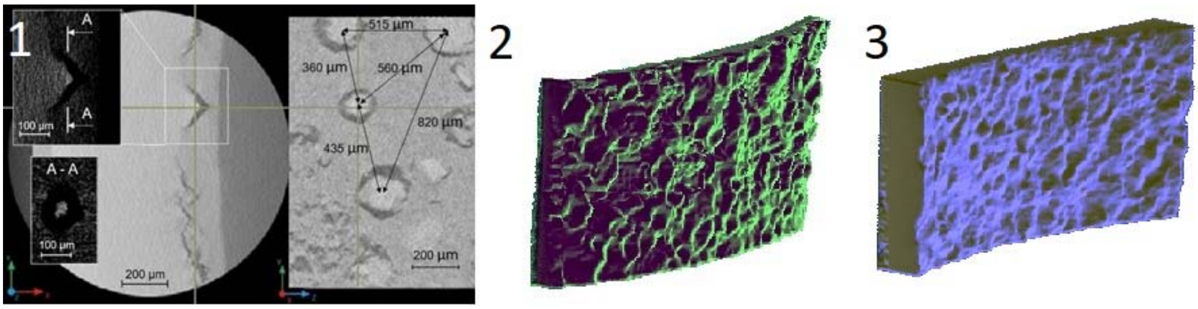

Fig. 10. (1) Orthogonal view of 1.4 µm voxel size in the X-ray tomography image of Zircaloy-2 tube oxidized at 1373 K in air for 0.5 h; left – transversal slice showing inner oxide, substrate metal, voids and cracks at the metal/oxide interface, and void magnification; right – arrangement of voids at the metal/oxide interface. The right image is a rotation of the left image by 90° around the yellow vertical line. The cross-section A-A presents dimensions of the bright void zone. (2) 3D view of the metal/oxide interface, a green image is the oxide layer at the interface. Many dents are spotted in the area of voids present at the metal side. (3) 3D view of the metal/oxide interface, a blue image is a metal side at the interface with visible voids

The average size of the bright zone at the top is around 70 µm, as shown in cross-section A-A. Based on analysis of the substrate surface under the internal oxide layer, about four such brighter zones can be found per 1 mm^2. The voids are spaced apart by an average distance of around 550 µm. Fig. 10 also presents an arrangement of bright deformations and cracks at the metal/inner oxide interface.

Figure 11 shows the X-ray tomography images of the oxidized tube (images 1 and 2) and the reference non-oxidized sample (image 3). Image 2, created by modifying the brightness and contrast of the image 1, presents the surfaces of the specimen after oxide removal. The arrangement of voids and cracks shown in image 1 corresponds to the bright zones in image 2. The top part of image 1 presents an open crack which exposes a base metal to the environment. Around 70% of all voids spotted on the inner surface of the tube caused the cracking of the oxide layer. The open crack created a hole of about 50 µm.

The appearance of voids may be associated with creation of vacancies and their diffusion at high temperatures. The concentration of vacancies in a substrate metal depends exponentially on temperature. The vacancies diffuse from the metal bulk to the interface between metal and ceramic oxide, and their further diffusion into the oxide layer is seriously stopped because of low diffusion rate in the oxide. At such conditions, two processes may occur. At first, the vacancies form small voids (or nodules in the presence of hydrogen, which may originate from the wet air). Further, they develop into here observed (macro)voids resulting in loss of cohesion between oxide and substrate, an occurrence of some bulges and an apparent increase in oxide thickness.

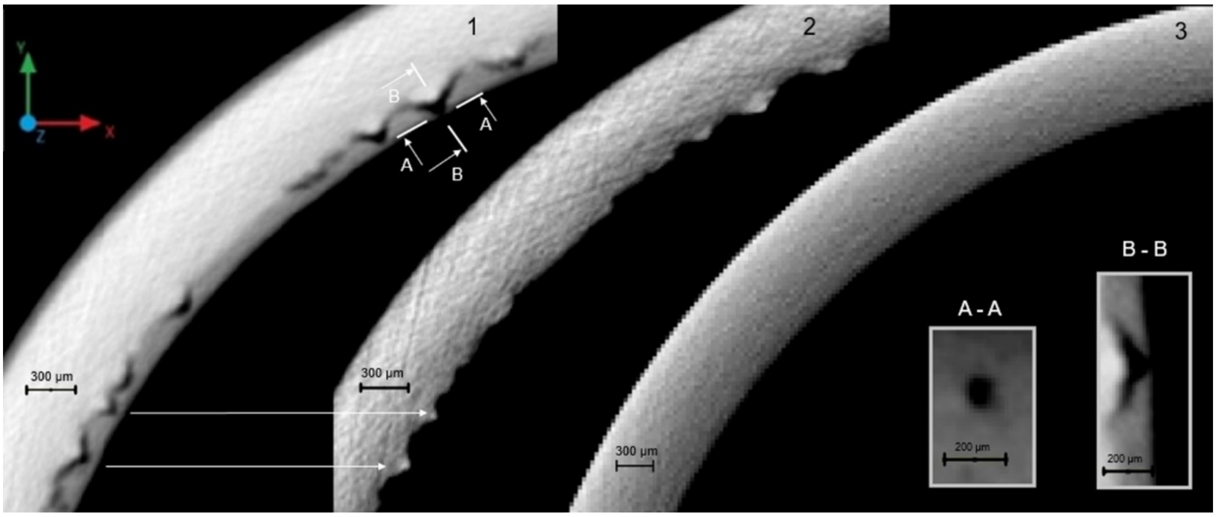

Fig. 11. 14 µm voxel size X-ray tomography image of the Zircaloy-2 tube oxidized at 1373 K in air for 0.5 h: (1) a transverse slice of the oxidized sample showing outer oxide, base metal, and inner oxide layer; (2) edited image 1 showing base metal without any oxides; (3) a transverse slice of the non-oxidized sample. Cross-sections A-A and B-B present open crack area visible in image 1, at different magnification

As illustrated by the image 2 in Fig. 12, the cracks along the metal/oxide interface correspond in length to the thickness of the inner oxide layers. The maximum cracks` openings are about 50 µm. The 3D geometry of the cracks is shown in image 3. The original surface before oxidation is approximately marked in image 2.

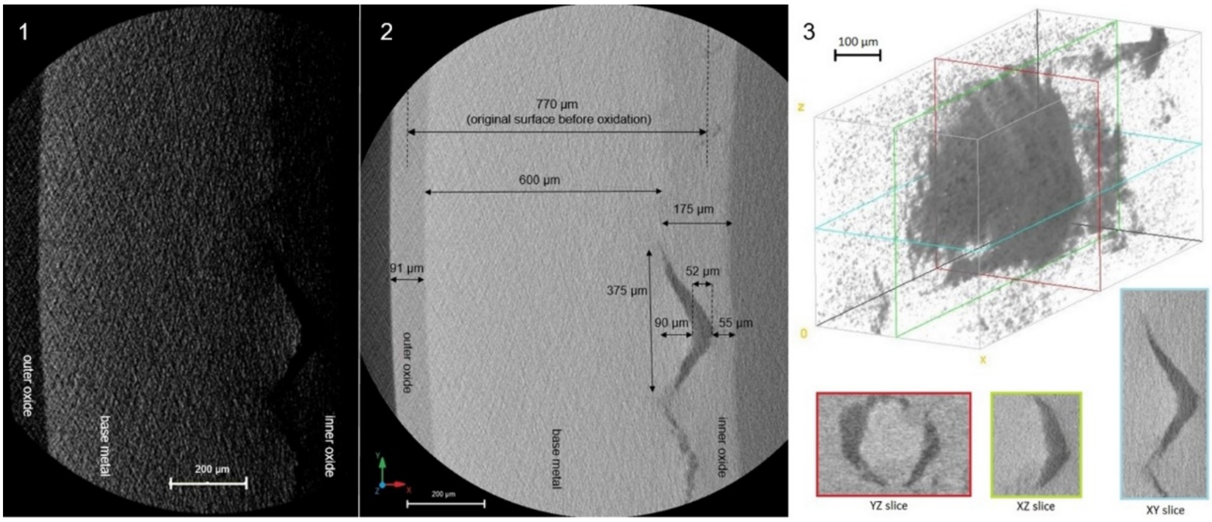

Fig. 12. 1.4 µm voxel size X-ray tomography image of the Zircaloy-2 tube oxidized at 1373 K in air for 0.5 h: (1) geometry of oxidized sample with adjusted brightness and contrast; (2) oxidized sample with shown dimensions of inner oxide, base metal, outer oxide layer, and crack present at the metal/oxide interface; (3) geometry of crack appearing at the metal/inner oxide interface

The evolution of many branched cracks into only few much longer cracks with increasing temperature is related to two factors: kinetic transition of crystalline oxide structure [4,5,25,37] and disappearance of monoclinic phase. The transition from (sub-)parabolic to faster, linear kinetics was found for the zirconium alloys as about or below 1320 K [4], just between both here applied temperatures. The inner oxide layers of specimens oxidized at 1373 K had no signs of cracking except the sample cooled in air, for which a single long crack initiated the top edge and propagated along the samples circuit right under top edge oxide. Crack is visible in Fig. 12 in the overall 3D image (1). The oxide microstructure evolves from relatively dense to porous oxide layer that does not enhance the initiation of cracks.

The following scenario of oxidation of Zircaloy-2 tube exposed for 30 minutes to ambient air at 1373 K can be proposed. On the outer surface of the tube, a uniform oxide scale with a smooth interface is formed without severe degradation such as detachment and only few deep cracks. The evolution on the inner surface is dramatically different. At the early stage of the oxide growth, heterogeneous oxidation a 1373 K becomes active. This heterogeneity may be attributed to formation of clusters of SPPs as already described [1,23,27,33,37-39]. The local oxidation kinetics is significantly decreased by the presence of such clusters and results in the formation of conic-like voids. The matrix around them undergoes oxidation and expands in the oxide growth direction, which causes the formation of a crack on the top of the unoxidized precipitates. The last step is the formation of a cylindrical hole at the top of the crack. Based on previous examinations, the bright zones visible at the void tops may be identified as clusters of SPPs. The absence of local bright zones on the outer surface may be attributed to more homogeneous microstructure of the smooth oxide/metal interface. The clustering of SPPs would be responsible for the interface waviness. It is also remarkable that the oxide thickness above void top is comparable to that on the outer surface. It means that if the SPP`s characteristics were the same in the inner and outer surface of the tube, the oxide scales would have the same thickness and no cracking would develop. The source of non-uniform distribution of SPPs may be related to metallurgical process at manufacturing the claddings.

All samples here examined showed cracks on the tops of voids. The example of such damage was described in [40] as a multi-layer spalled-off oxide. After passing the breakaway temperature region, the oxide scale formed at higher temperatures becomes protective again and forms a columnar structure. The inner compact oxide is split or tends to split; a possible reason could be the cool-down and heat-up cycle during combined quenching.

On the other hand, a thin oxide layer created under the detached zone generates lower stress in the α-layer and decreases the possibility of through-wall cracking. Such breakaway oxidation and spalling were already observed [15] and correspond to present results, in particular in 30% of the surface covered by spalled and the detachment zone about 5 mm long. The presence of large cracks perpendicular to the oxide surface, sometimes over 200 μm, twice the length of the neighboring oxide layer, was also already reported [4,25]. Moreover, the thickness of the oxide layer with present cracks was observed [41] as even three times thicker than that of the no-cracked layer and exceeded 300 μm.

Nodular oxidation was observed only for samples oxidized at 1373 K on the outer oxide surface. Figure 13 illustrates the nodule within the oxide layer, which differs in color. The specimens oxidized at 1373 K demonstrated the black oxide layers with white oxides surrounding nodular corrosion area. That means that in this are the phase transformation has not been completed and both oxides, monoclinic (white) more prone to cracking and detachment, and tetragonal (black) less permeable to oxygen appear together.

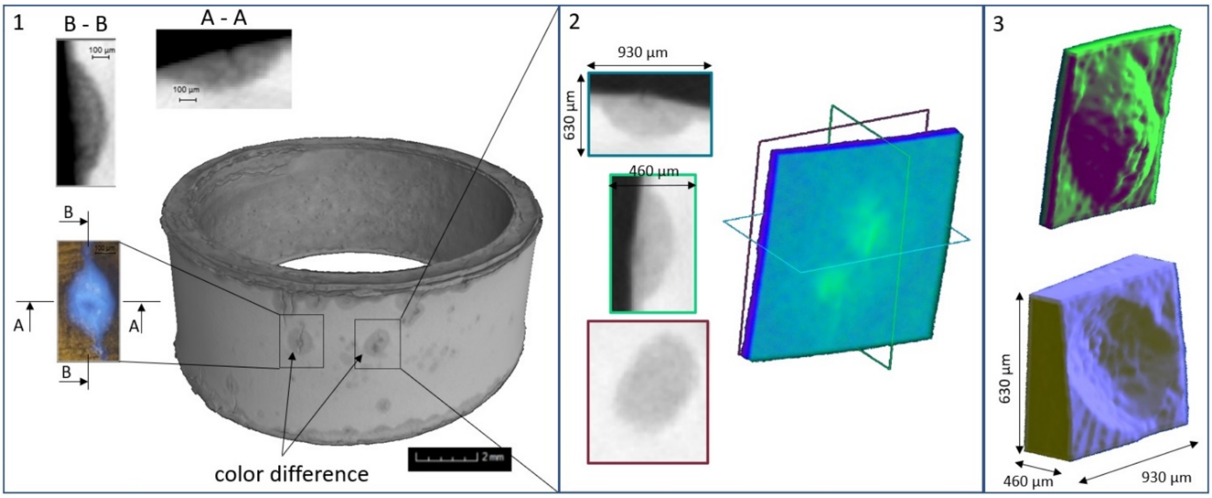

Fig. 13. (1) overall 3D view of specimen oxidized at 1373 K in air for 30 min, cooled in air; arrows mark the white color oxides surrounding cracks; blue image on the left presents image of the crack and cross-sections A-A and B-B, obtained by polarized light microscopy; (2) 3D view of crack (nodular oxidation) on the overall 3D image; color framed pictures on the right represent cross-sections marked on the 3D model by color lines; (3) 3D illustrations of nodular type oxidation; green image shows oxide scale surrounding crack viewed on image 2; blue model represents cladding damage under nodular type oxide

Fig. 13 illustrates two areas marked as squares with shown nodular oxidation. The areas surround small cracks of length between 700 µm and 800 µm. Blue image on the left presents the marked cross-sections visualized by X-ray tomography. The crack is around 150 µm deep and is surrounded by the oxide that highly exceeds in thickness the neighboring uniform black oxide layer. The oxide in the crack zone is around 310 µm long, three times more than the thickness of a uniform oxide formed outside the crack zone. Images 2 and 3 in Fig. 13 represent a 3D model of the nodular oxide. The green model illustrates the oxide seen from ZrO_2/Zircaloy interface. Blue image shows the damage in the cladding caused by nodular oxidation.

Nodular corrosion is a specific type of damage. At a particular stage in the oxidation process, small lens-like spots of white oxide form are present together with uniform black oxide. These nodules grow both in diameter and depth at a much higher rate than the uniform oxide. The reason why nodules are formed instead of the uniform oxide has not been reasonably explained yet. As reported in [16,41], during oxidation in vapor, H_2O is dissociated on the surface, and O^{2-} ions diffuse through the oxide film toward the zirconium matrix. The oxygen ions react with zirconium at the metal/oxide interface, and electrons are produced. The low electrical conductivity of ZrO_2 causes migration of protons in preference to electron conduction. As the wet air, containing vapor, has been applied, at such temperatures the water molecules may quickly dissociate, hydrogen atoms can migrate producing gaseous H_2 at the metal/oxide interface. Some hydrogen atoms become accumulated at the ZrO_2/Zircaloy interface and the remaining hydrogen diffuse into the matrix. The pressure of the accumulated H_2 gradually increases.

When the H_2 pressure exceeds the pressure which the film can resist, the ZrO_2 layer breaks. Once the protective black film breaks, reaction with the fresh metal surface occurs and the non-protective oxide is formed. The occurrence of nodules in the zircaloys is also suggested as due to local inhomogeneities in the alloying additives content [42]. Some metallic oxides, like Fe oxides, are unstable in a corrosive environment and may transform to highly porous granular ZrO_2 layer giving direct access of H_2O to the underlying metal. Such a course of damage may also be explained by the nitrogen-related model [4]. Nitrogen form nitrides which may be oxidized or form oxide-nitride interstitial phases. The voids might appear as a consequence of oxidation of nitride and its effusion in gas form, but diffusion of NO, NO_2 or N_2O_3 through still non-permanent oxide barrier is small and can be more critical only at higher oxidation temperature.

CONCLUSIONS

The zirconium oxide growth rate observed here corresponds to the values previously reported after oxidation at 1273 K and is slightly lower after oxidation at 1373 K, likely because of the effect of stresses affecting the oxygen diffusion due to temperature and stress gradients, and oxide phase transition.

The damage of oxide layers manifests itself in a different form, depending on oxidation temperature. The cracks and detachment of oxide scale appear mainly after oxidation at 1273 K, and voids, cracks on the outer side and nodules – mainly after oxidation at 1373 K. The degradation form seems critically dependent on thermodynamic transformation and kinetics of processes occurring during oxidation, and their determinants.

The primary mechanisms contributing to degradation at 1273 K can involve the formation of surface cracks within the monoclinic phase likely due to rising longitudinal stresses, formation and oxidation of nitrides, and oxidation of second phase particles simultaneously subjected to the residual stresses and followed by initiation of cracks.

The active mechanisms during oxidation at 1373 K resulting in degradation can be formation and diffusion of vacancies, effects of tensile stresses present on the outer surface and enhancing the cracks` propagation, and decomposition of vapor followed by hydrogen diffusion into the substrate/oxide interface and formation of nodules.

The performed X-ray CT measurements cannot directly recognize the degradation mechanisms, but, on the other hand, it may explicitly determine the degradation form, effects of temperature and surface curvature (tube surface) on presence and intensity of particular degradation forms.

ACKNOWLEDGMENTS

The research has been performed under the programme of the Polish National Science Center as a part of the project entitled “Hydrogen degradation of oxidized zirconium alloys”, No. 2013/11/B/ST8/04328.

REFERENCES

1. Proff C., Abolhassani S., Lemaignan C., Oxidation behaviour of zirconium alloys and their precipitates – A mechanistic study. J. Nucl. Mater. 432 (2013) 222–238.
2. Allen T.R., Konings R.J.M., Motta A.T., Corrosion of zirconium alloys. [In] Comprehensive Nuclear Materials, R.J.M Konings. (ed.), Elsevier, Amsterdam, 2012, pp. 49-68.

3. Park K., Yang S., Ho K., The effect of high pressure steam on the oxidation of low-Sn Zircaloy-4 at temperatures between 700 and 900 °C. J. Nucl. Mater. 420 (2012) 39-48.
4. Steinbrück M., Böttcher M., Air oxidation of Zircaloy-4, M5 and ZIRLO cladding alloys at high temperatures. J. Nucl. Mater. 414 (2011) 276-285.
5. Coindreau C., Duriez C., Ederli S. : Air oxidation of Zircaloy-4 in the 600-1000 °C temperature range: Modeling for ASTEC code application. J. Nucl. Mater. 405 (2010) 207-215.
6. Selmi N., Sari A., Study of oxidation kinetics in air of Zircaloy-4 by in situ X-Ray diffraction. Adv. Mater. Phys. Chem. 3 (2013) 168-173.
7. Sawabe T., Sonoda T., Furuya M., Kitajima S., Kinoshita M., Tokiwai M., Microstructure of oxide layers formed on zirconium alloy by air oxidation, uniform corrosion and fresh-green surface modification. J. Nucl. Mater. 419 (2011) 310-319.
8. Gong W, Zhang H, Qiao Y., Tian H., Ni X., Li Z., Wang X., Grain morphology and crystal structure of pre-transition oxides formed on Zircaloy-4. Corr. Sci. 74 (2013) 323-331.
9. Harlow W., Ghassemi H., Taheri M.L., Determination of the initial oxidation behavior of Zircaloy-4 by in-situ TEM. J. Nucl. Mater. 474 (2016) 126-133.
10. Ishii Y., Sykes J.M., Microstructure of oxide layers formed on Zircaloy-2 in air at 450°C. Mater. High Temp. 17 (2014) 23-28.
11. Gosset D., Le Saux M.L., Simeone D., Gilbon D. : New insights in structural characterization of zirconium alloys oxidation at high temperature. J. Nucl. Mater. 429 (2012) 19-24.
12. Gosset D., Le Saux M.L., In-situ X-ray diffraction analysis of zirconia layer formed on zirconium alloys oxidized at high temperature. J. Nucl. Mater. 458 (2015) 245-252.
13. Baek J.H., Jeong Y.H., Breakaway phenomenon of Zr-based alloys during a high-temperature oxidation. J. Nucl. Mater. 372 (2008) 152-159.
14. Yamato M, Nagase F, Amaya M., Reduction in the onset time of breakaway oxidation on Zircaloy cladding ruptured under simulated LOCA conditions. J. Nucl. Mater. 445 (2014) 78-83.
15. Fettré D., Favergeon J., Bouvier S., Detection of breakaway for a high-temperature oxidation of pure zirconium using acoustic emission correlated to thermogravimetry. Oxid. Met. 87 (2017) 367–379.
16. Kim H.G., Kim I.H., Choi B.K., Park Y.Y., A study of the breakaway oxidation behavior of zirconium cladding materials. J. Nucl. Mater. 418 (2011) 186-197.
17. Kim H.H., Kim J.H., Moon J.Y., Lee H.S., Kim J.J., Chai Y.S., High-temperature oxidation behavior of Zircaloy-4 and Zirlo in steam ambient. J. Mater. Sci. Technol. 26 (2010) 827-832.
18. Zienkiewicz N., Paradowska J., Serbinski W., Gajowiec G., Hernik A., Zielinski A., Oxidation and hydrogen behavior in Zr-2Mn alloy. Adv. Mater. Sci. 18 (2018) 37-48.
19. Annand K., Nord M., Maclaren I., Gass M., The corrosion of Zr(Fe, Cr)2 and Zr2Fe secondary phase particles in Zircaloy-4 under 350 °C pressurised water conditions. Corr. Sci. 128 (2017) 213-223.
20. Park D.J., Park J.Y., Jeong J.H., Microstructural analysis and XPS investigation of nodular oxides formed on Zircaloy-4. J. Nucl. Mater. 412 (2011) 233-238.
21. Lee C.M., Mok Y.K., Sohn D.S. : High-temperature steam oxidation and oxide crack effects of Zr-1Nb-1Sn-0.1Fe fuel cladding. J. Nucl. Mater. 496 (2017) 343-352.
22. Nikulin S.A., Rogachev S.O., Rozhnov A.B., Gusev A.Yu., Malgin A.G., Abramov N.N., Zharotsheva K.S., Khatkevich V.M., Koteneva M.V., Li E.V., The mechanism and kinetics of the fuel cladding failure during loading after high-temperature oxidation. J. Nucl. Mater. 452 (2014) 102-109.

23. Ni N., Lozano-Perez S., Sykes J.M., Smith G.D.W., Grovenor C.R.M., Focussed ion beam sectioning for the 3D characterisation of cracking in oxide scales formed on commercial ZIRLO™ alloys during corrosion in high temperature pressurised water. Corr. Sci. 53 (2011) 4073-4083.
24. Ni N., Lozano-Perez S., Sykes J., Grovenor C. : Multi-scale characterisation of oxide on zirconium alloys. Mater. High. Temp. 29 (2014) 166-170.
25. Steinbrück M., Vér N., Große M., Oxidation of Advanced Zirconium Cladding Alloys in Steam at Temperatures in the Range of 600–1200 °C. Oxid. Met. 76 (2011) 215-232.
26. Favergeon J., Montesin T., Mechano-Chemical Aspects of High Temperature Oxidation: A Mesoscopic Model Applied to Zirconium Alloys. Met. Oxid. 64 (2005) 252-279.
27. Duriez C., Dupont T., Schmet B., Enoch F., Zircaloy-4 and M5® high temperature oxidation and nitriding in air. J. Nucl. Mater. 380 (2008) 30-45.
28. Zeng C., Ling Y., Bai Y., Zhang R., Dai X., Chen Y., Hydrogen permeation characteristic of nanoscale passive films formed on different zirconium alloys. Intl. J. Hydrogen Energy 41 (2016) 7676-7690.
29. Zieliński A., Cymann A., Gumiński A., Hernik A., Gajowiec G., Influence of high temperature oxidation hydrogen absorption and degradation of Zircaloy-2 and Zr 700 alloys. High Temp. Mater. Proc. 38 (2019) 8-15.
30. Yoo H.-I., Koo B.-J., Hong J.-O., Hwang I.-S., Yeong I.-H., A working hypothesis on oxidation kinetics of Zircaloy. J. Nucl. Mater. 299 (2001) 235-241.
31. Lee K. W., Hong S.I., Zirconium hydrides and their effect on the circumferential mechanical properties of Zr–Sn–Fe–Nb tubes. J. Alloys Cmpds 346 (2002) 302-307.
32. Kurpaska L., Jozwik I., Jagielski J., Study of sub-oxide phases at the metal-oxide interface in oxidized pure zirconium and Zr-1.0% Nb alloy by using SEM/FIB/EBSD and EDS techniques. J. Nucl. Mater. 299 (2001) 235-241.
33. De Gabory B., Motta A.T., Wang K., Transmission electron microscopy characterization of Zircaloy-4 and ZIRLO^{TM} oxide layers. J. Nucl. Mater. 456 (2015) 272-280.
34. Tejland P., Andrén H.-A., Origin and effect of lateral cracks in oxide scales formed on zirconium alloys. J. Nucl. Mater. 430 (2012) 64-71.
35. Guerain M., Duriez C., Grosseau-Poussard J.L., Mermoux M., Review of stress fields in zirconium alloys corrosion scales. Corr. Sci. 95 (2015) 11-21.
36. Baris S., Abolhassani Y.L., Chiu L., Evans H.E., (2018) Observation of crack microstructure in oxides and its correlation to oxidation and hydrogen-uptake by 3D FIB Tomography – case of Zr-ZrO_2 in reactor. Mater. High Temp. 35 (2018) 14-21.
37. Birchley J., Fernandez-Moguel L. : Simulation of air oxidation during a reactor accident sequence: Part 1 - Phenomenology and model development. Ann. Nucl. Energy. 40 (2012) 163-170.
38. Rudling P., Wikmark G.A., A unified model of Zircaloy BWR corrosion and hydriding mechanisms. J. Nucl. Mater. 265 (1999) 44-59.
39. Yilmazbayhan A., Breval E., Motta A.T., Comstock R.J., Transmission electron microscopy examination of oxide layers formed on Zr alloys. J. Nucl. Mater. 349 (2006) 265-281.
40. Steinbrück M., Birchley J., Boldyrev A.V., Goryachev A.V., Grosse M., Haste T.J., Hózer Z., Kisselev A.E., Nalivaev V.I., Semishkin V.P., Sepold L., Stuckert J., Vér N., Veshchunov M.S., High temperature oxidation and quench behaviour of Zircaloy-4 and E110 cladding alloys. Progr. Nucl. Energy 52 (2010) 19-36.

41. Kawashima N.K.S.H., Mechanism of zircaloy nodular corrosion J. Nucl. Mater. 119 (1983) 229-239.
42. Likhanskii V.V., Evdokimov L.A., Effect of additives on the susceptibility of zirconium alloys to nodular corrosion. J. Nucl. Mater. 392 (2009) 447-452.